Modeling bending of α-titanium with embedded polycrystal plasticity in implicit finite elements

Marko Knezevic [a,*], Ricardo A. Lebensohn [a], Oana Cazacu [b], Benoit Revil-Baudard [b], Gwénaëlle Proust [c], Sven C. Vogel [d], Michael E. Nixon [e]

[a] Materials Science and Technology Division, Los Alamos National Laboratory, Los Alamos, NM 87545, USA
[b] Department of Mechanical and Aerospace Engineering, University of Florida, REEF, 1350 N Poquito Road, Shalimar, FL 32539, USA
[c] School of Civil Engineering, University of Sydney, NSW 2006, Australia
[d] Los Alamos Neutron Science Center, Los Alamos National Laboratory, Los Alamos, NM, USA
[e] Air Force Research Laboratory, Munitions Directorate, Eglin AFB, FL 32542, USA

ARTICLE INFO

ABSTRACT

An accurate description of the mechanical response of α-titanium requires consideration of mechanical anisotropy. In this work we adapt a polycrystal self-consistent model embedded in finite elements to simulate deformation of textured α-titanium under quasi-static conditions at room temperature. Monotonic tensile and compressive macroscopic stress–strain curves, electron backscattered diffraction and neutron diffraction data are used to calibrate and validate the model. We show that the model captures with great accuracy the anisotropic strain hardening and texture evolution in the material. Comparisons between predictions and experimental data allow us to elucidate the role that the different plastic deformation mechanisms play in determining microstructure and texture evolution. The polycrystal model, embedded in an implicit finite element code, is then used to simulate geometrical changes in bending experiments of α-titanium bars. These predictions, together with results of a macroscopic orthotropic elasto-plastic model that accounts for evolving anisotropy, are compared with the experiments. Both models accurately capture the experimentally observed upward shift of the neutral axis as well as the rigidity of the material response along hard-to-deform crystallographic $<c>$ direction.

© 2012 Elsevier B.V. All rights reserved.

1. Introduction

Titanium and titanium alloys constitute an important class of metals with widespread applications, ranging from aerospace, to medical applications, to consumer products, due to their outstanding properties such as high specific strength, good formability, good corrosion resistance and biocompatibility. Pure titanium (α-Ti) has a hexagonal close-packed (hcp) crystal structure. Hcp single crystals are known to exhibit strong mechanical anisotropy. The mechanical response of polycrystalline α-Ti aggregates is also highly anisotropic with marked tension–compression asymmetry, mainly due to pronounced texture (non-random distribution of crystal orientations), which is a consequence of thermo-mechanical processing. The complete sets of elasto-plastic anisotropic properties associated with all possible textures for α-Ti have theoretically been identified [1,2]. Grain morphology was also found to play a major role in anisotropy of α-Ti [3]. The behavior of α-Ti is further complicated by a wide variety of plastic deformation mechanisms with different activation stresses, which evolve differently with deformation, giving rise to anisotropic macroscopic hardening. A large number of studies have

been performed to identify the deformation mechanisms that are active under quasi-static deformation of pure α-Ti at room temperature. The experimental data reported concern the mechanical response and microstructure evolution under various loadings, including plane-strain compression and simple shear [4], uniaxial and biaxial tension [5], uniaxial compression [4,6], equal-channel angular extrusion [7], and rolling [8]. It was established that $\{10\bar{1}0\}\langle\bar{1}2\bar{1}0\rangle$ prismatic $<a>$ slip is the easiest glide mode in α-Ti. This was attributed to its c/a ratio of 1.587, which is lower than the ideal c/a ratio of 1.633. $(0001)\langle\bar{1}2\bar{1}0\rangle$ basal $<a>$ slip also operates in α-Ti but require higher activation stresses than the prismatic systems, or elevated temperatures [9]. $\{10\bar{1}1\}\langle\bar{1}\,\bar{1}23\rangle$ pyramidal $<c+a>$ slip systems are also harder than prismatic slip, but offer the additional degrees of freedom necessary to accommodate arbitrary plastic strains.

In addition to slip, these studies also reported occurrence of two main deformation twinning modes in α-Ti. The $\{10\bar{1}2\}\langle10\bar{1}\bar{1}\rangle$ tensile twinning and the $\{11\bar{2}2\}\langle11\bar{2}\bar{3}\rangle$ compressive twinning modes result in tensile and compressive strains along the parent grain's c-axis, respectively, and re-reorient the latter by 84.8° about the $\langle11\bar{2}0\rangle$ direction and by 64.6° about the $\langle1\bar{1}00\rangle$ direction, respectively [10]. Due to these microstructural changes, twinning has a profound influence on texture evolution and strain hardening of the material during plastic deformation [4,11]. In addition,
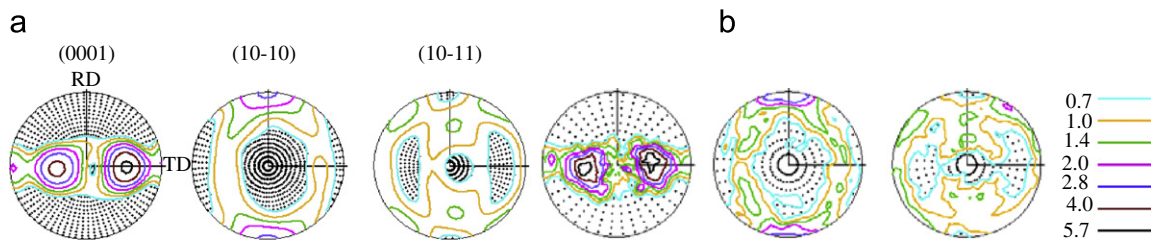
Fig. 1. (a) Pole figures measured by neutron diffraction showing the initial texture in the as-annealed α-titanium plate, and (b) Pole figures measured by EBSD showing the initial textures in the as-annealed α-Ti plate.

primary twins can favorably reorient a crystal for secondary and, subsequently, even for ternary twinning. The occurrence of these second- and third-generation twins in high-purity α-Ti and their influence on the mechanical behavior, especially under dynamic loadings was recently reported [6].

Three competing effects are generally accepted to explain the significant contribution of deformation twinning to strain hardening: (i) the texture hardening due to crystal reorientation, from softer to harder [12], (ii) the Hall–Petch effect due to grain subdivision [13], and (iii) the Basinski hardening mechanism due to transmutations of dislocations from glissile to sessile [14]. Thus, a realistic description of the mechanical behavior and microstructure evolution of α-Ti requires accurate twinning models. Four different approaches were proposed to address this outstanding problem and incorporated in crystal plasticity based constitutive laws: (i) the predominant twin reorientation (PTR) method [15], (ii) the volume fraction transfer (VFT) scheme [16], (iii) the total Lagrangian approach [17], and (iv) the composite-grain method [18]. All these methods were implemented within crystal plasticity models to account for microstructure evolution. Models such as Taylor-type [19–21] and self-consistent-type [22,23] have been rigorously formulated and widely used to understand and predict the mechanical response and microstructure evolution in metals subject to finite strains. The incorporation of crystal plasticity models into finite-element (FE) codes has also received substantial attention. For a detailed overview, the reader is referred to [24]. In particular, the strategy for embedding the viscoplastic self-consistent (VPSC) model in an implicit FE framework in the commercial FE code ABAQUS was presented in [25]. However, FE calculations where a polycrystalline aggregate is associated with each FE integration point are computationally extremely expensive, thus limiting its applicability to problems that do not require a fine spatial resolution. In view of applications to detailed analyses of complex forming processes for which the FE meshes are routinely of the order of thousands of elements, a robust macroscopic level elastic/plastic model are useful. The predictive capabilities of such a model can be assessed not only by comparison with experimental data but also through comparison with simulations using advanced polycrystalline models.

In the present paper, we demonstrate that using the VPSC framework the main features of the mechanical response of high-purity α-Ti are captured with very good accuracy. The plastic deformation mechanisms during monotonic tension and compression tests along different orientations are identified based on comparison with a comprehensive set of characterization data collected using electron backscattered diffraction (EBSD) and neutron diffraction. Due to the lack of reliable single-crystal data, the VPSC material parameters are calibrated based on stress–strain macroscopic response in monotonic tension and compression.

We first show that the VPSC model is able to reproduce stress–strain response and microstructure evolution for all orientations. Validation of the VPSC model is provided by applying it to testing conditions that were not used for the identification of the material parameters. To this end, simulations of the three-dimensional deformation of α-Ti beams subjected to four-point bending along different directions with respect to the hard-to-deform crystallographic $<c>$ axis predominant orientation of the material are presented.

Furthermore, we compare the simulation results in bending obtained by FE-VPSC to the results obtained using the analytic macroscopic yield criterion proposed in [23] coupled with a new distortional hardening model. It is shown that the accuracy of the results obtained with the macroscopic model is comparable to those obtained with the polycrystal model. We show that both models predict with great accuracy the evolution of tension-compression asymmetry of the material and the rigidity of the response along the crystallographic $<c>$ direction. Quantitative agreement with experimental data is presented. Specifically, the shifts of the neutral axis of the beams and changes in the cross-section geometry during deformation are well captured. Such a comparison is important in view of structural and process modeling applications.

2. Material and experiments

The starting material used in the present work is high-purity (99.999%), single-phase α-Ti. The material was supplied in the form of a 15.87 mm thick cross-rolled disk of 254 mm. The aggregate exhibits equiaxed twin-free grain structure with an average grain size of about 20 µm [12]. Fig. 1 shows the initial macro-texture measured by neutron diffraction at Los Alamos Neutron Science Center (LANSCE), and the initial micro-texture measured by electron back scattered diffraction (EBSD). The pole figures illustrate that the texture components of the measured micro-texture compare well with those of the macro-texture. The starting texture appears to be largely orthotropic, exhibiting strong (0001) intensity in the direction about 35° from TD. The $(10\bar{1}0)$ and $(10\bar{1}1)$ components tend to concentrate away from ND with one peak intensity for $(10\bar{1}0)$ at RD, and two peak intensities for $(10\bar{1}1)$ at about 60° from ND towards RD, and at 30° and 60° from RD and TD, respectively.

In a typical polycrystal plasticity simulation, a polycrystal is represented with a discrete set of grains (each having an orientation and a volume fraction) representative of the texture of the material. The discrete distribution of grains to be used in the simulations is constructed from the EBSD measurements. The measured texture is reduced to 500 weighted orientations chosen such as to reproduce the experimental textures shown in Fig. 1(b). The pole figures of the texture used as input in the simulations are essentially indistinguishable from the experimental ones depicted in Fig. 1(b), and are not shown.

Results of monotonic uniaxial tension and compression tests performed at a nominal strain rate of $10^{-3}\,\mathrm{s}^{-1}$ at room temperature, along the RD, TD, and ND directions were reported in [26], in which the effects of the direction and sense of loading on the macroscopic response of this material was studied. To gain understanding of the mechanisms responsible for the difference
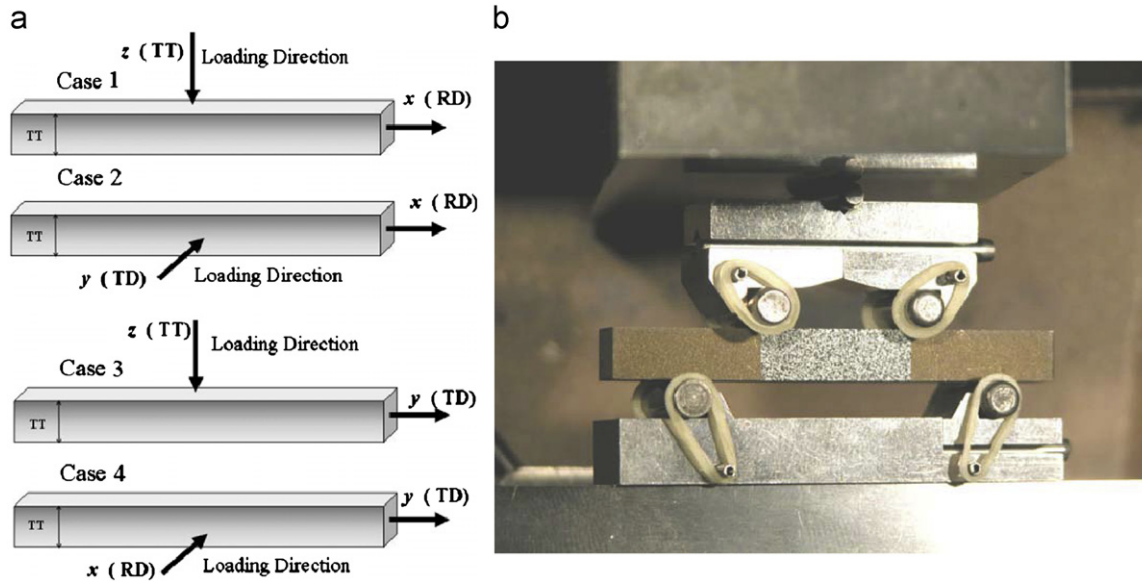
Fig. 2. (a) Four-point bending test specimen. The long axis of the specimens and the loading direction align with the symmetry directions of the α-Ti plate as indicated. (b) Four-point beam test jig with test specimen.

in hardening evolution between tension and compression, as well as to quantify texture evolution, compression tests to strain levels of 0.1, 0.2, 0.3, and 0.4 were also conducted and the macro-texture of the deformed samples was measured. In the present paper, we use this data to calibrate the material parameters of α-Ti, as required by the VPSC model. In addition, we present a set of new EBSD measurements that allow us to quantify twinning activity during deformation. The automated EBSD data collection was performed using an HKL system coupled to a Zeiss Ultra SEM at a voltage of 20 kV. The scans were run with a step size of 1 μm. This data is used to validate the VPSC model from the microstructure evolution perspective.

Four-point bending tests conducted on beams of the same material were reported in [27]. Because of the strong orthotropy of the material, four specimens were tested along different loading orientations. Specifically, two samples had the long axis aligned with the plate RD, while the other two samples had the long axis aligned with the plate TD. For each of these two sets of specimens, one sample was loaded in the TT direction while the other sample was loaded in the in-plane direction normal to the beam axis. These four test configurations are shown in Fig. 2(a). Each beam had a square cross-section of 6.35 mm × 6.35 mm and a length of 50.8 mm. The photograph of the four-point beam test jig with the test specimen is shown in Fig. 2(b). The experimental setup consisted of a pair of internal pins, moving downwards from top of the beam, and a pair of external pins, fixed underneath the beam. The internal and external pairs of pins were set at center-to-center distances of ± 6.35 mm and ± 19.05 mm, respectively. The total displacement of the upper pins was − 5.5 mm, corresponding to an axial (longitudinal) strain of the most external fiber of approxi-mately 0.2. The deformed specimens were cut at the midpoint and the final deformed cross-sections photographed. The photographed cross-sections are used to test the accuracy of the constitutive models presented in following sections of the paper.

3. Polycrystalline modeling

In order to model the mechanical behavior of polycrystalline α-Ti, we used a self-consistent model. This class of models is based on the solution of the problem of an ellipsoidal inclusion embedded in a homogenous effective medium. The inclusion is taken to be an individual grain while the homogenous medium represents the polycrystalline aggregate. A detailed description of the VPSC model used in this study can be found elsewhere [e.g. 22]. Here we only report the equations necessary to follow the details of the FE implementation of the model.

3.1. Single crystal and polycrystalline model

The constitutive relations between Cauchy stress deviator σ' and the viscoplastic strain-rate $\dot{\varepsilon}_{vp}$ at single-crystal level can be expressed as

$$\dot{\varepsilon}_{vp}(\mathbf{x}) = \sum_{k=1}^{N_k} m^k(\mathbf{x})\dot{\gamma}^k(\mathbf{x}) \ , \ \dot{\gamma}^k = \dot{\gamma}_o \left| \frac{\sigma' : m^k}{\tau_c^k} \right|^{1/m} sign\left(\sigma' : m^k \right) \quad (1)$$

where the sum runs over all N_k slip and twin systems and m^k is the Schmid tensor associated with slip or twinning system k. Plastic deformation in each grain occurs via the activation of both slip and twin modes. The corresponding slip or twin shear rate, $\dot{\gamma}^k$ on system k is given by the power-law. In the shear rate equation, $\dot{\gamma}_o^k$ represents the reference slip rate on system k, m is the rate sensitivity parameter, and τ_c^k is the resistance of slip or twinning system k. The rate-sensitivity exponent of 0.1 is taken to be the same for all slip and twinning modes. Consistent with the experimental evidence presented latter, the prismatic and pyr-amidal $<c+a>$ slip modes, and the tensile twinning modes are considered as potential systems for accommodating the imposed plastic strain. As mentioned earlier, compressive twinning also operates in α-Ti. However, we found that in the material under investigation this twinning mode was active only as a secondary twinning mode (i.e. compressive twins within the primary tensile twins, and, for simplicity, we did not consider compressive twinning in the present simulations.

A linear relation (an approximation of the actual local non-linear relation, Eq. (1) is assumed between $\dot{\varepsilon}_{vp}^{(r)}$ and $\sigma'^{(r)}$, i.e.

$$\dot{\varepsilon}_{vp}^{(r)} = \boldsymbol{M}^{(r)} : \boldsymbol{\sigma}'^{(r)} + \dot{\boldsymbol{\varepsilon}}^{o(r)} \quad (2)$$

where $\boldsymbol{M}^{(r)}$ and $\dot{\boldsymbol{\varepsilon}}^{o(r)}$ are the linearized viscoplastic compliance and back-extrapolated strain-rate of grain (r), respectively. The behavior of the single crystals can be homogenized assuming a linear relation
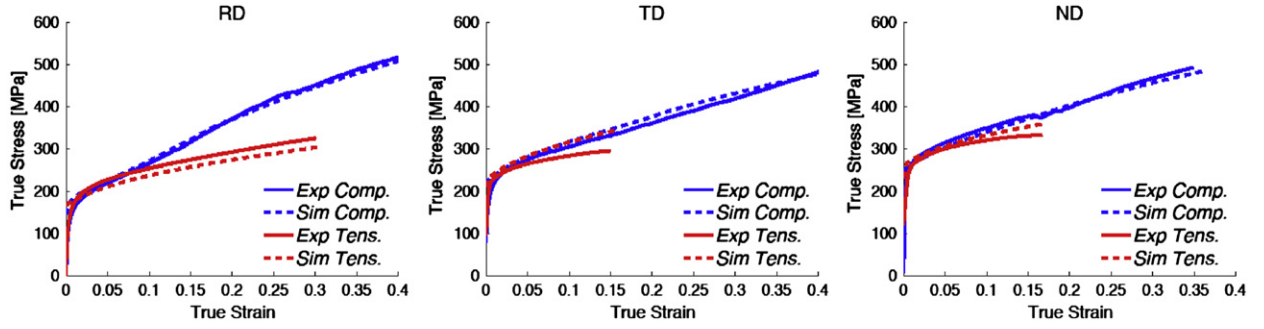
Fig. 3. Uniaxial tension and compression tests at room temperature on annealed samples of α-titanium along the direction indicated in the plots: measured (solid lines) and predicted (dashed lines) response.

at the effective medium (polycrystal, *px*) level

$$\dot{\boldsymbol{\varepsilon}}_{vp}^{(px)} = \boldsymbol{M}^{(px)} : \boldsymbol{\sigma}'^{(px)} + \dot{\boldsymbol{\varepsilon}}^{o(px)} \tag{3}$$

where $\dot{\boldsymbol{\varepsilon}}_{vp}^{(px)}$ and $\boldsymbol{\sigma}'^{(px)}$ are the effective (polycrystal) deviatoric strain-rate and stress tensors and $\boldsymbol{M}^{(px)}$ and $\dot{\boldsymbol{\varepsilon}}^{o(px)}$ are now the linearized viscoplastic compliance and back-extrapolated strain-rate of an a priori unknown homogeneous medium that represents the behavior of the polycrystal. The usual procedure to obtain the homogenized response of a linear polycrystal is the linear self-consistent method. The problem underlying the self-consistent method is that of a single crystal *r* of moduli $\boldsymbol{M}^{(r)}$ and $\dot{\boldsymbol{\varepsilon}}^{o(r)}$, embedded in a medium of moduli $\boldsymbol{M}^{(px)}$ and $\dot{\boldsymbol{\varepsilon}}^{o(px)}$, which can be obtained using standard self-consistent analysis.

All slip systems or twin variants *k*, within one mode α (or family) in a grain are assumed to exhibit the same resistance. The evolution of the resistance for each slip and twin mode in each grain *r* with accumulated shear strain is based on an extended Voce law [28]

$$\tau_c^{*k(r)} = \tau_{oo}^k + \left(\tau_1^k + \theta_1^k \Gamma^{(r)}\right)\left(1 - \exp\left(-\Gamma^{(r)}\left|\frac{\theta_o^k}{\tau_1^k}\right|\right)\right) \tag{4}$$

where $\Gamma^{(r)}$ is the total accumulated shear in the grain; $\tau_{oo}^k, \tau_1^k, \theta_o^k$ and θ_1^k are the initial threshold stress, initial hardening-rate, asymptotic hardening-rate and back-extrapolated threshold stress, respectively. In addition, we allow for self and latent hardening using the coupling coefficients $h^{kk'}$, which empirically account for the obstacles that new dislocations (or twins) with system k' create for the propagating of dislocations (or twins) on system *k*. The increase in the threshold stress is calculated as

$$\Delta\tau_o^{k(r)} = \frac{d\tau^{*k(r)}}{d\Gamma^{(r)}}\sum_{k'} h^{kk'}\dot{\gamma}^{k'(r)}\Delta t \tag{5}$$

In this work we handle twinning reorientation by means of the Predominant Twin Reorientation Scheme (PTR) [16]. In the PTR scheme, twinning is treated as a pseudo-slip mechanism. It differs from slip in its directionality, which means that activation is allowed only if the resolved shear stress is positive (for details, see [20]).

The above polycrystalline model is used to predict stress–strain response and microstructure evolution of the polycrystalline α-Ti by applying the viscoplastic deformation to the polycrystal in incremental steps.

3.2. Calibration of VPSC parameters for α-Ti

The determination of the parameters involved in the crystal plasticity model was based on polycrystalline Ti mechanical tests. Data on α-Ti single crystals (e.g. such as presented in [29] for pure Al olygocrystals or in [30] for Fe−3%Si single crystals) would serve for further verification/cross-validation of the single-crystal

Table 1
Slip mode hardening parameters.

Parameters	$\alpha = 1, \{10\bar{1}0\}\langle\bar{1}2\bar{1}0\rangle$	$\alpha = 2, \{10\bar{1}1\}\langle\bar{1}\,\bar{1}23\rangle$
τ_0^α (MPa)	98.	224.
τ_1^α (MPa)	41.	73.
θ_0^α	385.	300.
θ_1^α	75.	73.
$h^{\alpha\beta}, \ \beta = 1$	1.	1.
$h^{\alpha\beta}, \ \beta = 2$	1.5	0.7
$h^{\alpha\beta}, \ \beta = 3$	7.8	8.3

Table 2
Tensile-twin mode hardening parameters.

Parameters	$\alpha = 3, \{10\bar{1}2\}\langle\bar{1}011\rangle$
τ_0^α (MPa)	136.
τ_1^α (MPa)	80.
θ_0^α	4600.
θ_1^α	0.
$h^{\alpha\beta}, \ \beta = 1$	0.87
$h^{\alpha\beta}, \ \beta = 2$	1.
$h^{\alpha\beta}, \ \beta = 3$	10.

plasticity model as well as for verification of the homogenization procedure/boundary conditions. Fig. 3 compares the measured and predicted stress–strain responses in compression and tension along the three mutually perpendicular directions of the α-Ti plate. The stress–strain responses confirm the strong anisotropy and asymmetry exhibited by α-Ti in its plastic response. Axial tension and compression up to 40% strain is simulated by imposing 0.4% strain increments along the corresponding direction, while enforcing zero average stress along the two lateral directions of the sample. The hardening parameters calibrated in this paper are given in Tables 1 and 2 for the slip modes and the twin mode, respectively. It is seen that the hardening parameters successfully reproduce the measured mechanical response during the compressive loading and reasonably well reproduce those corresponding to the tensile loading. We note that the model captures well this characteristic increase in the work hardening rate associated with twinning activity in the RD compressed samples. The implication is that both the twining model and the hardening parameters are reasonable.

The concave shape in the early portion of the RD compression curve is an indication of deformation twinning-dominated deformation while the decrease in the work hardening rate in the later portion of the curve is a sign that twinning is exhausted and that the plastic deformation is dominated by slip or secondary twinning. In contrast, the RD tension curve exhibits a classical
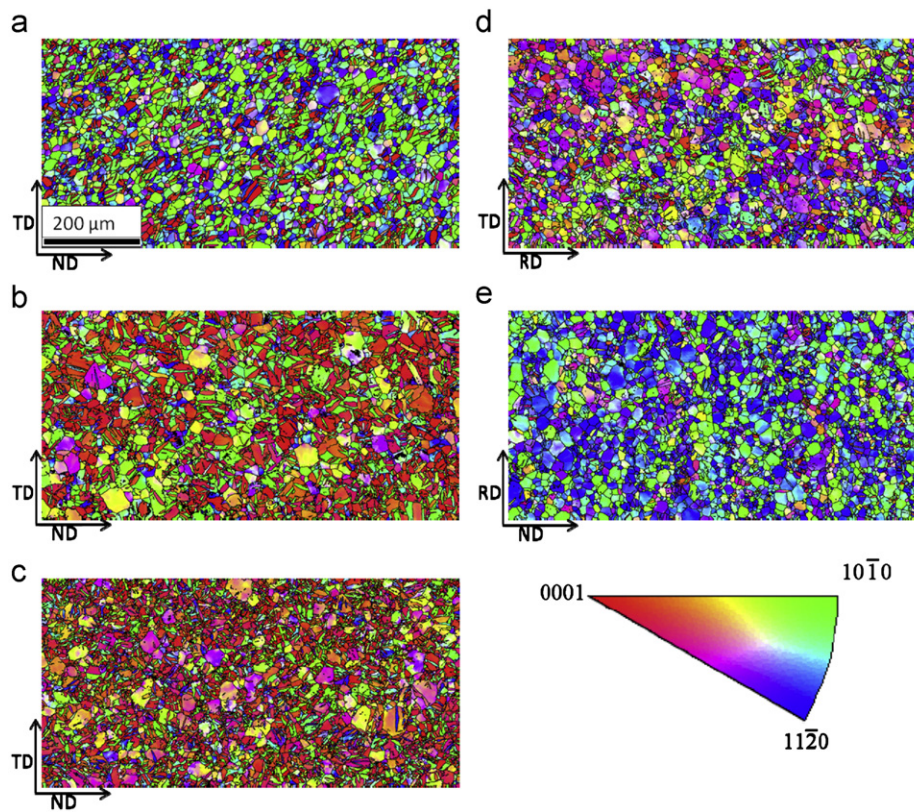
Fig. 4. Inverse pole figure (IPF) maps showing microstructure evolution in the α-titanium samples. (a) RD-compressed samples to true strain levels of 0.1, (b) 0.2 and (c) 0.3. (d) ND-compressed sample to a true strain of 0.1 and (e) TD-compressed to a true strain of 0.2. The colors in these maps indicate the orientation of the compression axis with respect to the crystal reference frame. All the maps are at the same magnification and therefore the scale bar on figure (a) is valid for all the maps. (For interpretation of the references to color in this figure caption, the reader is referred to the web version of this article.)

decreasing work hardening rate, which indicates that plastic deformation is dominated by slip. It is therefore not surprising to observe the increasing tension-compression asymmetry in the material response along RD. The TD and ND stress–strain curves do not exhibit the characteristics of twinning-dominated deformation but show rather constant or decreasing work-hardening rates. It is seen that the initial yield stress of the ND samples is higher than that of the TD samples, which is higher than the of the RD samples. This is indication that in ND samples a large fraction of grains require activation of the relatively hard pyramidal slip.

Microstructure evolution was investigated by EBSD in the samples compressed to several different strain levels. Fig. 4 shows the EBSD maps for the RD-compressed samples to strain levels of 0.1, 0.2 and 0.3, for the ND-compressed sample to a strain of 0.1, and for the TD-compressed sample to a strain of 0.2. From the maps obtained for the three RD-compressed specimens we can qualitatively estimate that the amount of twinning increases as a function of strain. The grains are steadily reorienting such that their c-axis become aligned with the loading direction, as it is clear from the increase of the red crystallographic orientations present in the maps. Analysis of the twins in the maps revealed that the misorientation between the twinned regions and the parent grain is approximately 85° about $\langle 11\bar{2}0 \rangle$, indicating that the predominantly active twin mode is tensile twinning. Although the initial texture is not favorably oriented for compressive twinning, we also observed a small fraction of these twins at the strain of 0.3. The occurrence of compressive twins can be understood in terms of tensile twins favorably oriented for secondary $\{11\bar{2}2\}\langle 11\bar{2}\bar{3} \rangle$ twinning In the TD- and ND-compressed samples the amount of twins is substantially smaller than in the RD-compressed samples. The tensile twin volume

fractions were measured from these maps and used for validation of the model.

Fig. 5 shows the comparison between the measured and predicted texture evolution. The pole figures reveal a dramatic texture change during the RD compression. We note that tensile twins play a dominant role in the texture evolution of the RD compressed samples and give rise to a texture component consisting of the basal poles distributed around the plate's RD. We note less texture evolution during TD and ND compression, compared to RD compression. Pole figures show a decrease in the (0001) intensity at about 35° from TD, relative to the starting texture. Consequently, as can be observed in the pole figures, other texture components are present. We attribute these changes in the pole figures of the RD- and TD-compressed samples to be mainly due to the slip activity.

Accurate predictions of the mechanical response and texture evolution is an indication that the predicted relative activities of the slip and twin modes contributing to plastic deformation are reasonable. The relative activity plots of the six deformed samples are shown in Fig. 6. The predicted deformation modes show substantial activity of deformation twinning in the material, which is consistent with the experimental observations. The volume fraction of twinned material in the RD-compressed sample goes up to 80% at a strain of 0.4. Deformation twins, while growing and accommodating plastic strain, reorient grains from softer to harder orientations inducing texture hardening related to the activation of hard pyramidal slip. We note the increase in the pyramidal slip activity during the RD compression. In contrast, it is predicted that in RD tension, strain is completely accommodated by slip. The twin volume fraction in the TD and ND compressed samples is predicted to be about 25% and 15%,
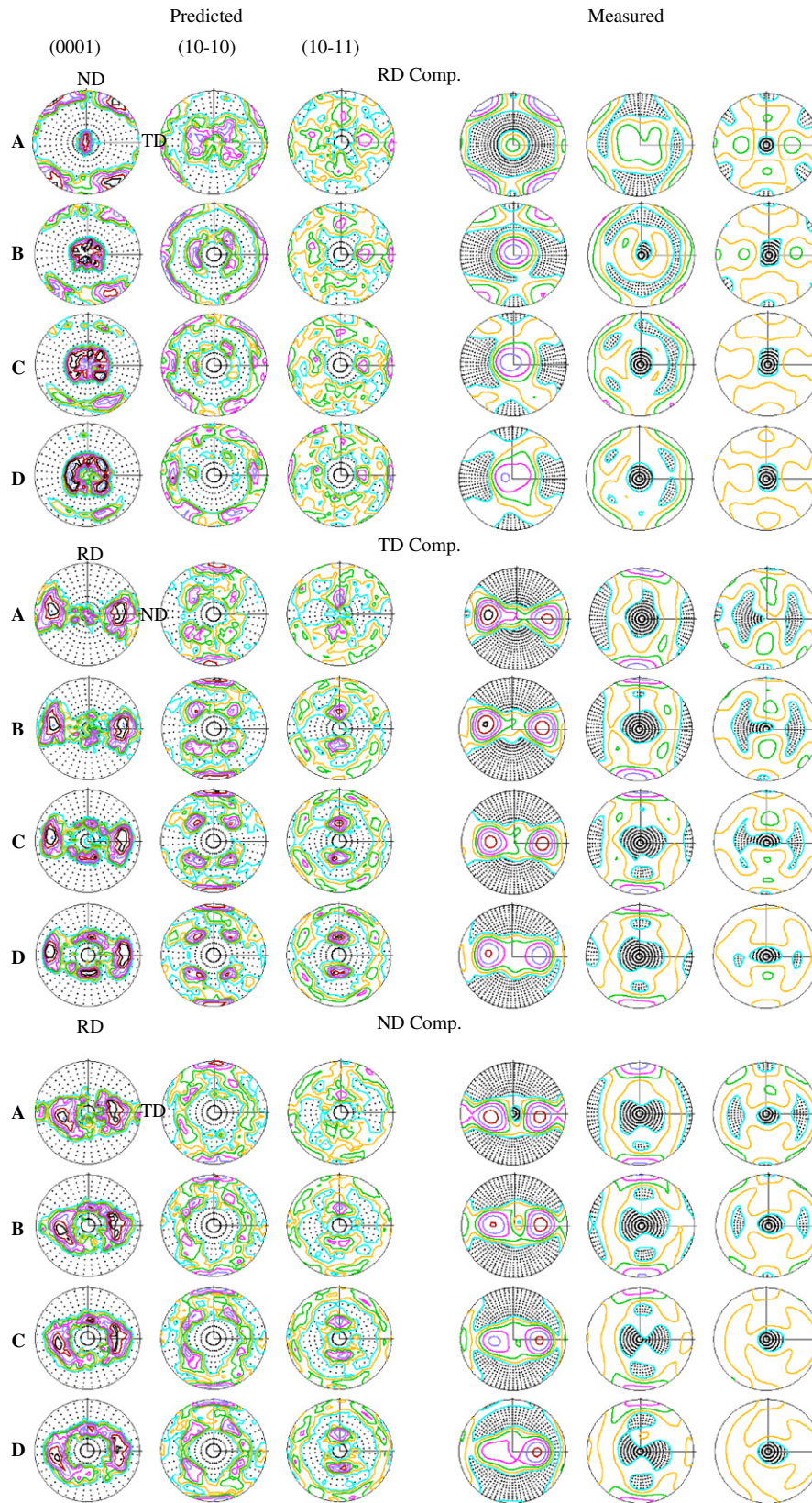
Fig. 5. Pole figures showing predicted (left) and measured (right) texture evolution in the α-titanium samples deformed along the directions indicated in the figure, up to true strains of (A) 0.1, (B) 0.2, (C) 0.3, and (D) 0.4. The compression axis is in the center of all the pole figures shown here.

respectively, at a strain of 0.4. We note substantial activity of the pyramidal slip during ND compression. This is expected since the large fraction of the grains was initially oriented with their *c*-axis

parallel to ND. The respective initial resistance of the pyramidal slip mode was calibrated to be 224 MPa (see Table 1). Compared with the initial twin mode resistance (see Table 2) of 136 MPa,
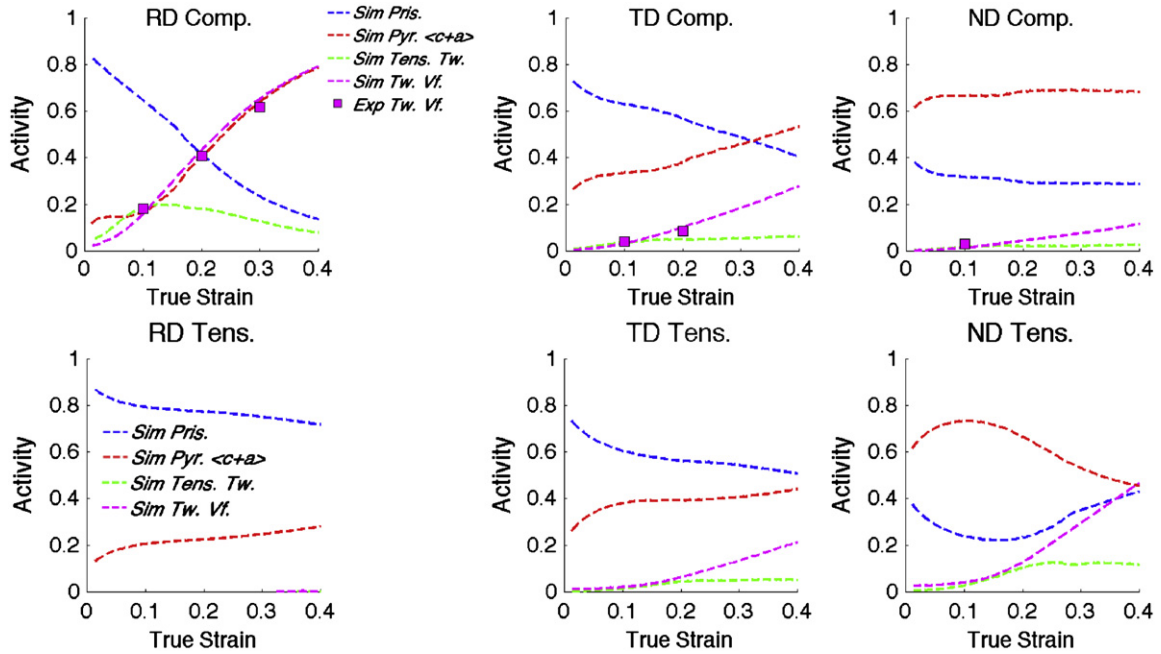
Fig. 6. Predicted relative activities of each deformation mode contributing to plasticity of α-titanium samples deformed in compression and tension as a function of strain. Also plotted is the evolution of twin volume fraction in the samples predicted by VPSC (lines) and measured by EBSD (symbols).

and the initial prismatic slip mode resistance of 98 MPa (see Table 1), it is the hardest deformation mode in α-Ti.

The predicted and measured evolution of twin volume fractions are also compared in Fig. 6 for the three compression samples. Discrete points representing the measured twinned volume fractions are superimposed over the lines representing predicted twinned volume fractions. We regard the match as very good. In the model, we account for the texture hardening due to twinning explicitly by reorienting the grains. In addition, the morphological features of the twins in α-Ti suggests that the hardening induced by the Hall–Petch type effects and Basinski cannot be ignored. We account for these mechanisms empirically using the latent hardening matrix $h^{\alpha\beta}$. The fact that the model captures the highly anisotropic mechanical behavior of α-Ti quite well confirms our reasoning.

Considering that the PTR model represents a simplified scheme for treating twinning compared to e.g. the composite grain model [18], and considering that we use a rather simple hardening law compared to some more sophisticated laws based on dislocation densities such as in [31,32], we regard the match between experimental and simulated stress–strain response and the resulting microstructure evolution as very good. The final goal of the present paper is to use this VPSC model within the FE code ABAQUS to predict geometrical changes of the components made of α-Ti. The corresponding methodology and results are presented in what follows.

4. Embedding of a self-consistent crystal plasticity model in implicit finite elements

The strategy of embedding the VPSC model at meso-scale level in an implicit FE framework was discussed in [25]. A finite element integration point is considered as a polycrystalline material point, whose meso-scale mechanical response is obtained interrogating the VPSC model. As a result, we introduce another level of homogenization from the meso-scale to the macro-scale. In the implementation of VPSC as a User Material Subroutine (UMAT) in ABAQUS-Standard, the total strain

increment $\Delta\boldsymbol{\varepsilon}$ is divided into the elastic $\Delta\boldsymbol{\varepsilon}_{el}$ and viscoplastic $\Delta\boldsymbol{\varepsilon}_{vp}$ parts as

$$\Delta\boldsymbol{\varepsilon} = \Delta\boldsymbol{\varepsilon}_{el} + \Delta\boldsymbol{\varepsilon}_{vp} = \boldsymbol{C}^{-1} : \Delta\boldsymbol{\sigma} + \Delta\boldsymbol{\varepsilon}_{vp} \tag{7}$$

where $\boldsymbol{C}$ is the elastic stiffness of the polycrystalline material point, $\Delta\boldsymbol{\sigma}$ is the Cauchy stress increment, and $\Delta\boldsymbol{\varepsilon}_{vp} = \Delta\boldsymbol{\varepsilon}_{vp}(\boldsymbol{\sigma})$ is computed using the VPSC model for each polycrystalline material point.

In the earlier work [25], the VPSC calculations were performed in a local co-rotational frame and the texture was represented in this moving frame. In this work we introduce a change in such a way that the polycrystalline material undergoes the macroscopically imposed rotation at every time increment, in addition to a rotation due to the plastic spin and anti-symmetric part of the Eshelby tensor. The benefit of the new implementation is that the field variables are always calculated and always stay in the global frame.

The macro-scale constitutive model is formulated incrementally using

$$\dot{\boldsymbol{\sigma}} = \boldsymbol{C} : (\dot{\boldsymbol{\varepsilon}} - \dot{\boldsymbol{\varepsilon}}_{vp}) \tag{8}$$

Integrating Eq. (8) from time t to $t+\Delta t$ gives

$$\dot{\boldsymbol{\sigma}}\Delta t = \boldsymbol{C} : (\Delta\boldsymbol{\varepsilon} - \Delta\boldsymbol{\varepsilon}_{vp}) \tag{9}$$

At macroscopic level, the applied load is divided in increments, and the equilibrium at each increment is obtained by means of the FE analysis in an iterative fashion, using a global non-linear solver. The load increment is controlled by time. Once the problem has being solved at time t, the solution for the next time increment requires the polycrystal model to provide a tangent stiffness (Jacobian) matrix $\boldsymbol{C}^{tg} = \partial\Delta\boldsymbol{\sigma}/\partial\Delta\boldsymbol{\varepsilon}$ for each material point, in order for the FE scheme to compute an initial guess for the nodal displacements at $t+\Delta t$. The strain increments obtained from that prediction at each material point, $\Delta\boldsymbol{\varepsilon}^{FE}$, together with the stress $\boldsymbol{\sigma}^t$ and the set of internal state variables corresponding to the previous increment, are used inside UMAT to calculate a new guess for the stress and the Jacobian at $t+\Delta t$. When convergence in stress equilibrium is achieved by the global non-linear scheme, the new values (at $t+\Delta t$) of the stresses, the internal variables, and the Jacobian matrix are accepted for every node, and the calculation advances to the next

increment. For a given $\Delta\boldsymbol{\varepsilon}^{FE}$, the VPSC-based UMAT is based on the minimization procedure described in [25] and briefly summarized here.

The elastic constitutive relation for the stress in the material point at $t+\Delta t$

$$\boldsymbol{\sigma}^{t+\Delta t} = \boldsymbol{\sigma}^t + \boldsymbol{C} : \Delta\boldsymbol{\varepsilon}_{el} = \boldsymbol{\sigma}^t + \boldsymbol{C} : (\Delta\boldsymbol{\varepsilon} - \Delta\boldsymbol{\varepsilon}_{vp}) \qquad (10)$$

where $\boldsymbol{C}$ is the elastic stiffness of the polycrystal. In this context, the natural choice for $\boldsymbol{C}$ is to use the elastic self-consistent (ELSC) estimate. Note that an ELSC calculation for the determination of $\boldsymbol{C}$ is implemented in the VPSC code, at the beginning of each deformation increment. Hence, the textural changes are also accounted for in determining the elastic modulus of the poly-crystalline material element. The single-crystal elastic constants used for Ti were: $C_{11}=162.4$ GPa, $C_{12}=92.0$ GPa, $C_{13}=69.0$ GPa, $C_{33}=180.7$ GPa and $C_{44}=46.7$ GPa.

Using Eq. (10) and the viscoplastic constitutive relation, we obtain

$$\Delta\boldsymbol{\varepsilon} = \boldsymbol{C}^{-1} : \Delta\boldsymbol{\sigma} + \Delta t \; \dot{\boldsymbol{\varepsilon}}_{vp}^{(px)}(\boldsymbol{\sigma}^t + \Delta\boldsymbol{\sigma}) \qquad (11)$$

For a given trial strain increment $\Delta\boldsymbol{\varepsilon}^{FE}$ we define the residual $\boldsymbol{X}(\Delta\boldsymbol{\sigma})$ at each material point as a non-linear function of the stress increment $\Delta\boldsymbol{\sigma} = \boldsymbol{\sigma}^{t+\Delta t} - \boldsymbol{\sigma}^t$

$$\boldsymbol{X}(\Delta\boldsymbol{\sigma}) = \Delta\boldsymbol{\varepsilon} - \Delta\boldsymbol{\varepsilon}^{FE} = \boldsymbol{C}^{-1} : \Delta\boldsymbol{\sigma} + \Delta t \; \dot{\boldsymbol{\varepsilon}}_{vp}^{(px)}(\boldsymbol{\sigma}^t + \Delta\boldsymbol{\sigma}) - \Delta\boldsymbol{\varepsilon}^{FE} \qquad (12)$$

The condition $\boldsymbol{X}(\Delta\boldsymbol{\sigma})=0$ (i.e. $\Delta\boldsymbol{\varepsilon}=\Delta\boldsymbol{\varepsilon}^{FE}$), is enforced using a Newton–Raphson (NR) scheme to solve the non-linear system of equations. The corresponding Jacobian $\boldsymbol{J}_{NR}$ is given by

$$\frac{\partial\boldsymbol{X}(\Delta\boldsymbol{\sigma})}{\partial(\Delta\boldsymbol{\sigma})} = \boldsymbol{J}_{NR}(\Delta\boldsymbol{\sigma}) = \boldsymbol{C}^{tg} = \boldsymbol{C}^{-1} + \Delta t \; \frac{\partial\dot{\boldsymbol{\varepsilon}}_{vp}^{(px)}}{\partial(\Delta\boldsymbol{\sigma})}\left(\boldsymbol{\sigma}^t + \Delta\boldsymbol{\sigma} \; ; \; \beta_i^t\right)$$
$$= \boldsymbol{C}^{-1} + \Delta t \; \boldsymbol{M}^{(px)}(\boldsymbol{\sigma}^t + \Delta\boldsymbol{\sigma}) \qquad (13)$$

Hence, given a guess $\Delta\boldsymbol{\sigma}^{k-1}$ for the stress increment, the new guess is obtained as

$$\Delta\boldsymbol{\sigma}^k = \Delta\boldsymbol{\sigma}^{k-1} - \boldsymbol{J}_{NR}^{-1}\left(\Delta\boldsymbol{\sigma}^{k-1}\right) : \boldsymbol{X}\left(\Delta\boldsymbol{\sigma}^{k-1}\right) \qquad (14)$$

This approach provides a closed expression for the FE Jacobian as a function of the viscoplastic tangent moduli (calculated as part of the VPSC algorithm), the elastic stiffness of the aggregate, and the FE time increment. The use of this expression greatly reduces the overall computational cost because the polycrystal's stress and the elasto-viscoplastic tangent stiffness tensor are obtained from the same calculation loop. Moreover, the FE Jacobian allows for the quadratic convergence of the macroscopic non-linear equations.

5. Orthotropic elasto-plastic constitutive model

The above direct implementation of a polycrystal model into an advanced commercial FE code has the advantage that it follows the evolution of anisotropy and tension-compression asymmetry due to evolving texture. As mentioned earlier, these kinds of FE calculations are computationally very intensive. In view of applications to detailed analyses of complex forming processes, a robust macroscopic level elastic/plastic model is useful.

In the following, we present such a macroscopic formulation and further assess its ability to capture the evolving tension-compression asymmetry of the high-purity α-titanium material investigated by comparison with the VPSC simulation results for bending.

Recently, a macroscopic three-dimensional yield function that accounts for both the tension-compression asymmetry and aniso-tropy of high-purity α-titanium has been developed. While this yield function is briefly reviewed in the following, a detailed description can be found in [23]. The general form of the orthotropic yield

function is

$$\varphi\left(J_2^0, J_3^0\right) = [\left(J_2^0\right)^{3/2} - c J_2^0]^{1/3} \qquad (15)$$

where c is a material parameter that accounts for the tension-compression asymmetry while, $J_2^0 = (1/2) tr\left(\boldsymbol{\Sigma}^2\right)$ and $J_3^0 = (1/3) tr(\boldsymbol{\Sigma}^3)$ denote the second and the third invariant of the transformed stress tensor

$$\boldsymbol{\Sigma} = \boldsymbol{L} : \boldsymbol{\sigma} \qquad (16)$$

with σ the Cauchy stress tensor applied to the material. In Eq. (16), $\boldsymbol{L}$ is a fourth-order orthotropic and symmetric tensor ($\boldsymbol{L}_{ijkl} = \boldsymbol{L}_{jikl} = \boldsymbol{L}_{jilk} = \boldsymbol{L}_{klij}$, with $i,j,k,l=1,2,3$) that is traceless. This latter constraint ensures that yielding is insensitive to hydrostatic pressure. Modeling the anisotropy by means of the 4th order symmetric and orthotropic tensor $\boldsymbol{L}$, ensures that the material response is invariant under any orthogonal transformation belonging to the symmetry group of the material (i.e. rotations along the symmetry axes). Furthermore, the minimum number of independent anisotropy parameters that is needed such as to satisfy these symmetry requirements is intro-duced. The isotropic case is recovered when $\boldsymbol{L}$ is set equal to $\boldsymbol{I}_4$, the fourth-order symmetric identity tensor. Thus, the tensor $\boldsymbol{L}$ has six non-zero components in the ($\boldsymbol{x}$, $\boldsymbol{y}$, $\boldsymbol{z}$) coordinate system associated with the material symmetry axes (RD, TD and ND, respectively) and in Voigt notations is represented by a 6×6 matrix given by

$$\boldsymbol{L} = \frac{1}{3}\begin{bmatrix} a_2+a_3 & -a_3 & -a_2 & 0 & 0 & 0 \\ -a_3 & a_1+a_3 & -a_1 & 0 & 0 & 0 \\ -a_2 & -a_1 & a_1+a_2 & 0 & 0 & 0 \\ 0 & 0 & 0 & 3a_4 & 0 & 0 \\ 0 & 0 & 0 & 0 & 3a_5 & 0 \\ 0 & 0 & 0 & 0 & 0 & 3a_6 \end{bmatrix} \qquad (17)$$

The equivalent stress $\overline{\sigma}$, associated to the anisotropic criterion (15) is

$$\overline{\sigma} = A_1 \left(J_2^{3/2} - c J_3\right)^{1/3} \qquad (18)$$

where A_1 is a constant defined such that $\overline{\sigma}$ reduces to the tensile yield stress along RD, i.e.

$$A_1 = \frac{3}{[(a_2^2 + a_3^2 + a_2 a_3)^{3/2} - c(a_2 + a_3)a_2 a_3]^{1/3}} \qquad (19)$$

Due to the homogeneity of degree one in stresses of the yield criterion, we can set $a_1=1$ while the anisotropy coefficients, a_j with $j=2\ldots4$ and the parameter c associated with the tension-compression asymmetry of the material can be determined using the experimentally determined tensile and compressive flow stresses along the axes of symmetry of the material.

Since microstructural changes affect the asymmetric/anisotro-pic response of the material, all the materials parameters involved in the yield criterion (15) need to be updated as well. In [26], updating of the coefficients was done using linear interpolation between individual surfaces corresponding to a finite set of individual prestrains using the methodology proposed by [33]. In this paper, the orthotropic yield criterion developed in [26] is coupled with a new distorsional hardening model and applied to the description of the mechanical response of α-Ti in bending.

It is assumed that hardening is governed by a measure of equivalent plastic strain, $\overline{\varepsilon}^p$ associated to $\overline{\sigma}$ given by Eq. (18) using the work-equivalence principle [34]. Thus, yielding is described as

$$F(\sigma, \overline{\varepsilon}^p) = \overline{\sigma}(\sigma, \overline{\varepsilon}^p) - Y\left(\overline{\varepsilon}^p\right) \qquad (20)$$

where $Y(\overline{\varepsilon}^p)$ is a reference hardening curve (e.g. tensile stress–strain curve along RD). The latter can be approximated by

$$Y(\overline{\varepsilon}^p) = \beta \left(\varepsilon_0 + \overline{\varepsilon}^p\right)^n \qquad (21)$$

with $\beta = 377.8$ MPa, $\varepsilon_0 = 3.9 \times 10^{-4}$ and $n = 0.170$.

In order to model the difference in hardening rates between tension and compression loadings both the anisotropy coefficients and the strength-differential parameter c, are considered to evolve with accumulated plastic deformation. Specifically, using the experimental flow stress data, we determine parameter c and the anisotropy coefficients corresponding to initial yielding and several individual levels of equivalent plastic strains $\bar{\varepsilon}_p^1 < \bar{\varepsilon}_p^2 < \ldots < \bar{\varepsilon}_p^m$. Next, to obtain the anisotropy coefficients corresponding to any given level of accumulated plastic strain $\bar{\varepsilon}_p^j < \bar{\varepsilon} < \bar{\varepsilon}_p^{j+1}$, linear interpolation is used, i.e.

$$c(\bar{\varepsilon}) = \alpha(\bar{\varepsilon})c\left(\bar{\varepsilon}_p^j\right) + (1-\alpha(\bar{\varepsilon}))c\left(\bar{\varepsilon}_p^{j+1}\right)$$

and

$$a_k(\bar{\varepsilon}) = \alpha(\bar{\varepsilon})a_k\left(\bar{\varepsilon}_p^j\right) + (1-\alpha(\bar{\varepsilon}))a_k\left(\bar{\varepsilon}_p^{j+1}\right), \quad k = 2\ldots4 \qquad (22)$$

the interpolation parameter α involved in Eq. (22) being defined as

$$\alpha(\bar{\varepsilon}) = \frac{\bar{\varepsilon}_p^{j+1} - \bar{\varepsilon}}{\bar{\varepsilon}_p^{j+1} - \bar{\varepsilon}_p^j} \qquad (23)$$

The effective stress corresponding to $\bar{\varepsilon}$ is computed by substituting Eq. (22) into Eq. (18).

For the material studied, the numerical values of parameter c and of the anisotropy coefficients corresponding to initial yielding and four other individual levels of equivalent plastic strains (up to 0.2 strain) are given in Table 3, while Fig. 7 gives the theoretical yield surfaces for these pre-strain levels (solid lines) and that for intermediate pre-strain levels (interrupted lines).

Table 3
Yield criterion coefficients for high purity α-titanium corresponding to different values of prestrain $\bar{\varepsilon}^p$. Note that a_1 is set to 1 for all cases.

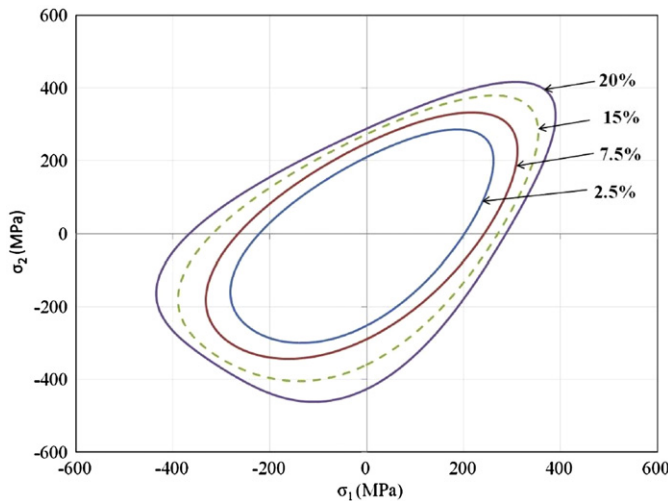| $\bar{\varepsilon}^p$	a_2	a_3	a_4	c
0.000	0.9186	1.9985	1.3286	-0.3975
0.025	0.9071	1.7270	1.3972	-0.4202
0.050	0.8343	1.6477	1.3651	-0.3422
0.075	0.8576	1.6193	1.4135	-0.3746
0.100	0.8902	1.6062	1.4490	-0.5142
0.200	0.9443	1.4246	1.4262	-0.9685

Fig. 7. Yield surfaces according to criterion (18) corresponding to $\bar{\varepsilon}^p = 2.5\%$, 7.5% and 20% (solid lines) and the yield surface at 15% with anisotropy coefficients and c calculated by interpolating between the respective coefficients for $\bar{\varepsilon}^p = 7.5\%$ and $\bar{\varepsilon}^p = 20\%$.

This J2-J3 orthotropic yield criterion, in conjunction with the distortional hardening model was implemented as a User Material Subroutine (UMAT) in the FE code ABAQUS. A fully implicit integration algorithm was used.

6. Bending of α-titanium

We simulate a set of four-point beam-bending experiments on the beams of α-Ti using the VPSC and J2-J3 models embedded in ABAQUS-Standard. Bending conditions were selected for cross-validation of the models capabilities to predict the effects of the directionality of twinning. Depending on the loading direction with respect to the $<c>$ axis of the grains, we expect to find qualitative differences between the response of the upper (top/compressive) and lower (bottom/tensile) fibers of the beam and a shift of the neutral axis, (by fiber we mean a thin volume of material, parallel to the longitudinal axis of the beam.) Four FE models were constructed corresponding to the four beam configurations tested (see Fig. 2). Two beams have the long axis along the rolling direction (RD) while the other two have the long axis along the transverse direction (TD). For each of these two sets of specimens, one beam was loaded in the through-thickness (TT) direction while the other sample was loaded in the in-plane direction normal to the beam axis. As a result, the beams had different starting textures relative to the bending plane. Our aim is to illustrate the ability of the models to capture the strong effect of texture-induced anisotropy and asymmetry on the geometrical changes during bending of α-Ti. As noticed earlier, the α-Ti plate exhibited orthotropic symmetry, and thus, we only model a quarter of the beam using a structured mesh of $20 \times 5 \times 3$ elements along the half-length, thickness and half-width, respectively by imposing symmetry boundary conditions. The displacement of the upper pins was modeled by imposing displacement of 5.5 mm along the loading direction to the upper nodes, located at 6.35 mm from the midpoint. The lower nodes, located at 19.05 mm from the midpoint are constrained along the loading direction (no displacement allowed along the loading direction) to represent the fixed pins. After performing a mesh-sensitivity study, we observe that further refinement of the mesh did not change the results. Introducing more elements only increased the computational time involved. We found that the quadratic elements with reduced integration (C3D20R) provided best compromise between accuracy of the simulations and the computational time involved. These elements were flexible to bend owing to the large number of degrees of freedom (20 nodes) and efficient owing to the reduced number of integration points where the computationally intensive polycrystalline response is obtained.

Input in the VPSC-based UMAT consisted of the initial texture of the α-Ti plate represented by 500 weighted orientations (see Fig. 1) at each material point and a set of the hardening parameters adjusted in this paper to reproduce the tension and compression response in three main directions of the plate (see Tables 1 and 2). Input in the J2-J3 UMAT consisted of the set of parameters given in Table 3.

The comparison of the simulated and measured final cross-sections for the four configurations is shown in Fig. 8. The views of the deformed beams show the strong effect that texture had on the final shapes. Note that when the through-thickness direction (TT) is perpendicular to the loading direction (Cases 2 and 4), cross-sections of the beams retain an almost square shape because they do not deform along the $<c>$ axis. Case 1 and Case 3 are similar to each other. The samples develop wedge-shape cross sections, with more lateral strain in Case 1 (RD of the plate is horizontal) than in Case 2 (when TD of the plate is horizontal). This is consistent with the uniaxial tests results of
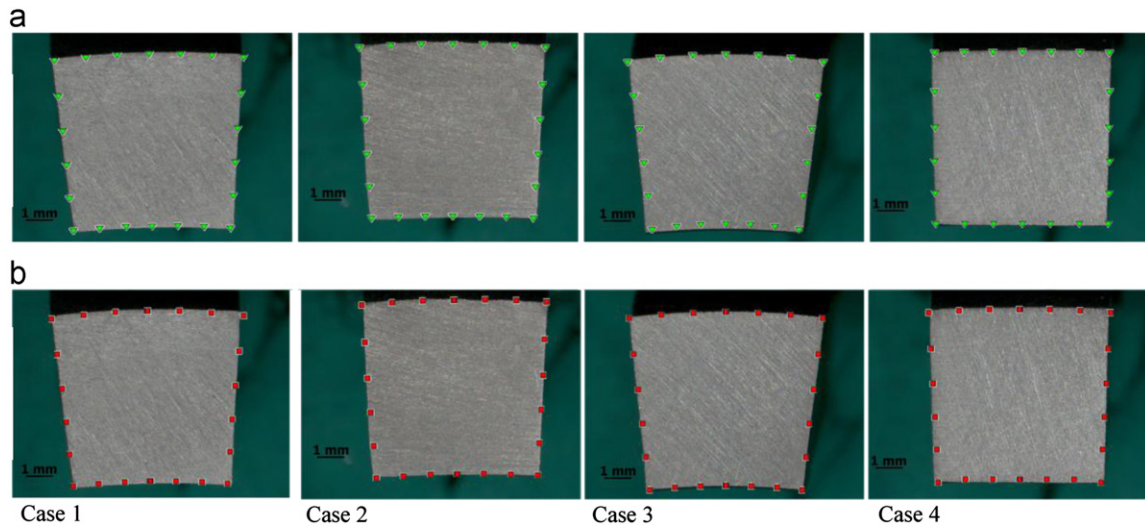
Fig. 8. Comparison of the predicted and measured cross-sections of the α-titanium beams. The external nodal coordinates of the deformed FEM models are superimposed on the photographed experimentally deformed beams. (a) Numerical predictions obtained by the VPSC UMAT, and (b) Numerical predictions obtained by the J2-J3 UMAT.
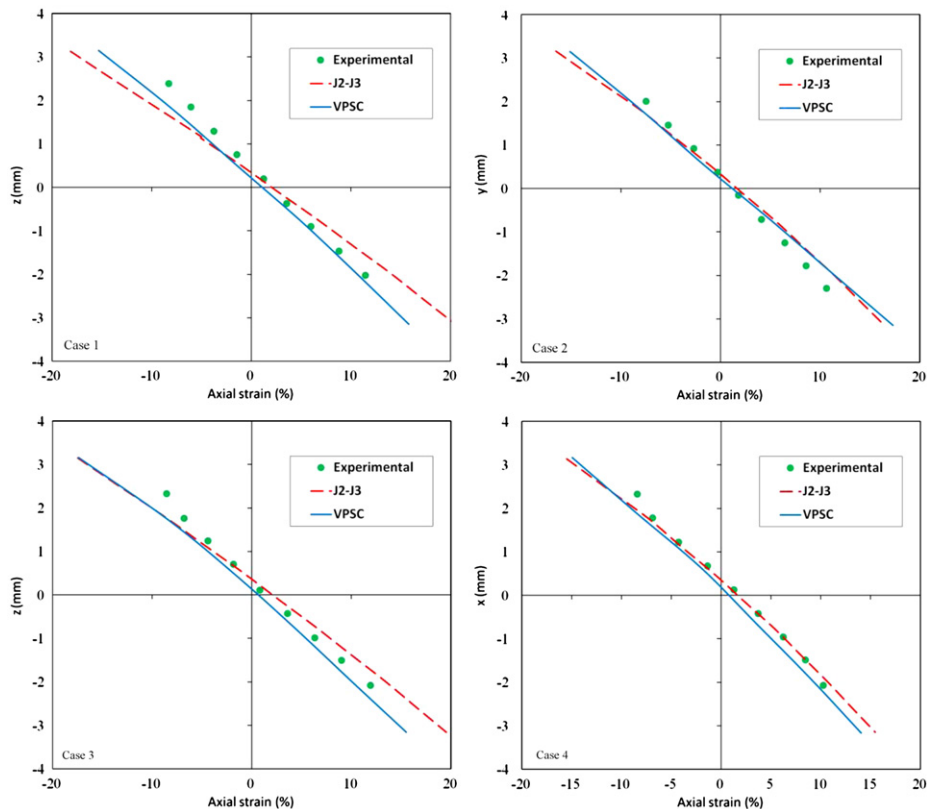

Fig. 9. Comparison of the axial strains along the height of the beams simulated with the VPSC UMAT and the J2-J3 UMAT with experiments. Note the shift in neutral axis of the beams.

Fig. 3 which show that for strain levels below 15%, the material's yield strength in the TD direction is higher than in the RD for both tensile and compressive loadings.

It is evident that the constitutive laws capture well the evolution of the strength differential effects resulting from more rapid hardening in the part of the beam undergoing compression, than in the part of the beam undergoing tension. Both models show an excellent agreement with the data. Comparison between the measured and simulated variation of the axial strain (strain along the axis of the beam) with the height of the beam, at the

center of the cross-section, is shown in the Fig. 9 for each case. Note the upward shift of the neutral axis, which is due to the material being softer in tension than in compression, is well described by both models.

Let us close this section mentioning some pros and cons of both formulations. On the one hand, the J2-J3 UMAT is about three orders of magnitude faster than the VPSC-based UMAT. On the other hand, while material constants established for a material system by the VPSC-based UMAT are valid for any initial texture, the analytic yield surface parameters require readjustment when a different initial

texture is considered. In this regard, the VPSC-based UMAT is more generic.

7. Conclusions

The deformation behavior of polycrystalline α-titanium was examined using experiments and crystal plasticity modeling. The mechanical response, characterized in tension and compression along the main plate directions, was highly anisotropic and exhibited strength-differential effects. Twinning statistics and texture evolution were determined based on EBSD and neutron diffraction data. The twin volume fraction in a sample deformed along RD to a strain of 0.3 was measured to be over 60%. We calibrated a crystal plasticity-based constitutive law to reproduce the stress–strain responses and texture evolution. The predicted deformation modes show substantial activity of twinning in RD compression. In particular, the twinning-dominated deformation appears in early stages. When twinning becomes exhausted, the slip-dominated deformation begins. This shift in the active deformation modes is reflected by the increasing and then decreasing work-hardening rate of the RD compression curve. In contrast, it is predicted that the RD tension curve is completely dominated by slip, and thus, exhibits a classical decreasing work hardening rate throughout. As a consequence, the RD response exhibits strong strength-differential effects. The TD and ND stress–strain curves show rather constant hardening rates.

In addition to reproducing the monotonic stress–strain responses and texture evolution for all the tests, we further challenged the predictive capabilities of the model implemented within the implicit finite-element framework. For this purpose, we used a VPSC-based UMAT to simulate a set of four-point bending experiments. We show that the model successfully captures the deformed shape of the beam cross-sections by direct comparison with experiments. Furthermore, we presented simulation results obtained with the macroscopic yield criterion and a new treatment of the distortional hardening model. We demonstrated the capabilities of this new J2-J3 model to capture the evolution of tension-compression asymmetry of the material, as well as the rigidity of the material response along hard to deform $<c>$ direction. The accuracy of the results obtained with the macroscopic model is similar to those obtained with the polycrystal model.

Acknowledgments

References

[1] T. Fast, M. Knezevic, S.R. Kalidindi, Comput. Mater. Sci. 43 (2008) 374–383.
[2] X. Wu, G. Proust, M. Knezevic, S.R. Kalidindi, Acta Mater. 55 (2007) 2729–2737.
[3] B.S. Fromm, B.L. Adams, S. Ahmadi, M. Knezevic, Acta Mater. 57 (2009) 2339–2348.
[4] A.A. Salem, S.R. Kalidindi, R.D. Doherty, Acta Mater. 51 (2003) 4225–4237.
[5] S. Zaefferer, Mat. Sci. Eng. A 344 (2003) 20–30.
[6] W. Tirry, M. Nixon, O. Cazacu, F. Coghe, L. Rabet, Scripta Mater. 64 (2011) 840–843.
[7] D.H. Shin, I. Kim, J. Kim, Y.S. Kim, S.L. Semiatin, Acta Mater. 51 (2003) 983–996.
[8] Y.B. Chun, S.H. Yu, S.L. Semiatin, S.K. Hwang, Mat. Sci. Eng. A 398 (2005) 209–219.
[9] S. Suwas, B. Beausir, L.S. Toth, J.J. Fundenberger, G. Gottstein, Acta Mater. 59 (2011) 1121–1133.
[10] M.H. Yoo, Metall. Mater. Trans. A 12 (1981) 409–418.
[11] A.A. Salem, S.R. Kalidindi, R. Doherty, S.L. Semiatin, Metall. Trans. A 37A (2006) 259.
[12] M. Knezevic, A. Levinson, R. Harris, R.K. Mishra, R.D. Doherty, S.R. Kalidindi, Acta Mater. 58 (2010) 6230–6242.
[13] S. Asgari, E. El-Danaf, S.R. Kalidindi, R.D. Doherty, Metall. Mater. Trans. A 28A (1997) 1781–1795.
[14] Z.S. Basinski, M.S. Szczerba, M. Niewczas, J.D. Embury, S.J. Basinski, Rev. Metall. Cah. Inf. Tech. 94 (1997) 1037–1044.
[15] P. Van Houtte, Acta Metall. Mater. 26 (1978) 591–604.
[16] C.N. Tomé, R.A. Lebensohn, U.F. Kocks, Acta Metall. Mat. 39 (1991) 2667–2680.
[17] X. Wu, S.R. Kalidindi, C. Necker, A.A. Salem, Acta Mater. 55 (2007) 423–432.
[18] G. Proust, C.N. Tomé, G.C. Kaschner, Acta Mater. 55 (2007) 2137–2148.
[19] S.R. Kalidindi, C.A. Bronkhorst, L. Anand, J. Mech. Phys. Solids 40 (1992) 537–569.
[20] M. Knezevic, H.F. Al-Harbi, S.R. Kalidindi, Acta Mater. 57 (2009) 1777–1784.
[21] J.B. Shaffer, M. Knezevic, S.R. Kalidindi, Int. J. Plas. 26 (2010) 1183–1194.
[22] R.A. Lebensohn, C.N. Tomé, P.P. Castaneda, Phil. Mag. 87 (2007) 4287–4322.
[23] R.A. Lebensohn, C.N. Tomé, Acta Metall. Mater. 41 (1993) 2611–2624.
[24] F. Roters, P. Eisenlohr, L. Hantcherli, D.D. Tjahjanto, T.R. Bieler, D. Raabe, Acta Mater. 58 (2010) 1152–1211.
[25] J. Segurado, R.A. Lebensohn, J. Llorca, C.N. Tomé, Int. J. Plas. 28 (2012) 124–140.
[26] M.E. Nixon, O. Cazacu, R.A. Lebensohn, Int. J. Plas. 26 (2010) 516–532.
[27] M.E. Nixon, R.A. Lebensohn, O. Cazacu, C. Liu, Acta Mater. 58 (2010) 5759–5767.
[28] C. Tomé, G.R. Canova, U.F. Kocks, N. Christodoulou, J.J. Jonas, Acta Metall. 32 (1984) 1637–1653.
[29] Z. Zhao, M. Ramesh, D. Raabe, A.M. Cuitiñño, R. Radovitzky, Int. J. Plas. 24 (2008) 2278–2297.
[30] B. Klusemann, B. Svendsen, H. Vehoff, Com. Mat. Sci. 52 (2012) 25–32.
[31] I.J. Beyerlein, C.N. Tomé, Int. J. Plas. 24 (2008) 867–895.
[32] M. Knezevic, L. Capolungo, C.N. Tomé, R.A. Lebensohn, D.J. Alexander, B. Mihaila, R.J. McCabe, Acta Mater. 60 (2012) 702–715.
[33] B. Plunkett, R.A. Lebensohn, O. Cazacu, F. Barlat, Acta Mater. 54 (2006) 4159–4169.
[34] R. Hill, J. Mech. Phys. Solids 35 (1987) 23–33.